

Characterization of Lipid Bilayers Adsorbed to Functionalized Air/Water Interfaces

Julio Pusterla^a, Ernesto Scoppola^b, Christian Appel^a, Tetiana Mukhina^a,
Chen Shen^c, Gerald Brezesinski^a and Emanuel Schneck^{a*}

^a Institute for Condensed Matter Physics, TU Darmstadt, Hochschulstrasse 8, 64289 Darmstadt, Germany.

^b Max Planck Institute of Colloids and Interfaces, Am Mühlenberg 1, 14476 Potsdam, Germany.

^c Deutsches Elektronen-Synchrotron DESY, Notkestrasse 85, 22607 Hamburg, Germany.

* Corresponding author: emanuel.schneck@pkm.tu-darmstadt.de

Keywords: Liquid Interfaces, Model Membrane, Surface Scattering, Bilayer Adsorption.

Abstract

Lipid bilayers immobilized in planar geometries, such as solid-supported or "floating" bilayers, have enabled detailed studies of biological membranes with numerous experimental techniques, notably x-ray and neutron reflectometry. However, the presence of a solid support also has disadvantages as it complicates the use of spectroscopic techniques as well as surface rheological measurements that would require surface deformations. Here, in order to overcome these limitations, we investigate lipid bilayers adsorbed to inherently soft and experimentally well accessible air/water interfaces that are functionalized with Langmuir monolayers of amphiphiles. The bilayers are characterized with ellipsometry, X-ray scattering, and X-ray fluorescence. Grazing-incidence X-ray diffraction reveals that lipid bilayers in a chain-ordered state can have significantly different structural features than regular Langmuir monolayers of the same composition. Our results suggest that bilayers at air/water interfaces may be well suited for fundamental studies in the field of membrane biophysics.

1. Introduction

Biological membranes are major components of all living organisms. They form the boundaries between the various compartments of cells and constitute platforms for essential biochemical processes like enzymatic reactions, molecular transport, and signal transduction^{1, 2}. To understand the details of these processes, structural insight is often a prerequisite. Over the last several decades, various experimental techniques, notably X-ray and neutron reflectometry and scattering, have enabled the structural characterization of lipid bilayers and more complex models of biological membranes at sub-nanometer resolution³⁻⁸. This approach has led to a considerable progress in our understanding of intramembrane molecular distributions^{3, 4}, interactions of membranes with drugs, water soluble proteins and other components of the aqueous medium⁵⁻⁷, and inter-leaflet lipid exchange dynamics⁸. All of this was only possible with the simultaneous development of methods for membrane immobilization in planar geometries, such as solid-supported membranes^{9, 10}, or membranes floating on polymers^{11, 12}, soft tethers^{13, 14}, or lipid bilayers¹⁵. However, the presence of a solid support has a number of disadvantages. At first, it prevents any investigations that involve surface deformations, such as interfacial dilatational rheology¹⁶ which would yield insights into the viscoelastic and mechanical membrane properties. Moreover, the presence of condensed bulk media on both sides of the membrane (the aqueous phase and the solid) exclude or at least complicate other measurement techniques, such as infrared spectroscopy^{17, 18}. Regarding surface x-ray diffraction for the study of crystalline ordering in lipid bilayers¹⁹, the absence of a solid support may widen the range of applicability towards a controlled variation of the area per lipid.

In the present work, we investigated lipid bilayers adsorbed to planar air/water interfaces that are functionalized with Langmuir monolayers of amphiphiles. The formation of these bilayers through the fusion of small unilamellar vesicles (SUVs) is promoted by electrostatic attraction. The interfacial layers were characterized by ellipsometry, various X-ray scattering techniques, and X-ray fluorescence which, in combination, provide a comprehensive structural picture of the surface-adsorbed bilayers. Bilayers in fluid (L_α) and in chain-ordered (L_β) phases were studied. The L_β phase of a lipid bilayer was characterized for the first time by

grazing-incidence X-ray diffraction at the air/water interface and the chain ordering was found to be significantly different from that in a regular Langmuir monolayer of the same composition.

2. Materials and Methods

2.1. Chemicals

The phospholipids 1,2-dimyristoyl-sn-glycero-3-phosphocholine (DMPC), 1,2-dimyristoyl-sn-glycero-3-phospho-1'-rac-glycerol (DMPG), 1,2-dipalmitoyl-sn-glycero-3-phosphoethanolamine (DPPE) and the cationic lipids 1,2-dimyristoyl-3-trimethylammonium-propane (DMTAP) and 1,2-stearoyl-3-trimethylammonium-propane (DSTAP) were purchased from Sigma-Aldrich (Merck KGaA, Germany). The fluorinated amphiphile 1H,1H-Perfluorooctadecan-1-ol (PFOL) was purchased from Proactive Molecular Research (USA) and the Perfluorooctadecanoic Acid (PFOA) from Santa Cruz Biotechnology, Inc (USA). High purity (99.5 –99.9%) NaCl was purchased from Sigma-Aldrich. Hexane, methanol, and chloroform were of the highest commercial purity available and were purchased from Sigma-Aldrich (Merck KGaA, Germany).

2.2. Sample preparation

The lipidic mixture of DPPE-DSTAP (70:30 mol%) was spread onto the air/water interface from a solution of chloroform-methanol (7:3, v/v) and the mixture of PFOL-PFOA (70:30 mol%) from a solution of hexane-ethanol (9:1, v/v). Pressure-area isotherms were recorded with a KSV NIMA Langmuir trough (KSV, Finland). Multilamellar vesicles (MLVs, 70:30 mol% of DMPC-DMTAP or DMPC-DMPG) were prepared by generating a uniform lipid film on the wall of a glass test tube by solvent evaporation under an N₂ stream from a lipidic solution in chloroform-methanol (7:3, v/v). Remaining traces of solvent were removed with a desiccator under vacuum for 2 hours. The dried lipids were then hydrated with water and subjected to three freezing–thawing cycles (–195°C and 40°C, respectively) to get MLVs. Finally, SUVs were prepared by extrusion (20 times, extruder set with holder/heating block from Avanti Polar Lipids, USA) of MLVs composed by DMPC-DMTAP or DMPC-DMPG through polycarbonate filters with 50 nm pore size, at room temperature.

2.3. Ellipsometry

A null ellipsometer (Multiskop, Optrel GbR, Germany) with a He-Ne laser ($\lambda = 632.8$ nm) was used to monitor lipid layer thicknesses at the air/water interface. The incident angle was set to 57° . The DPPE-DSTAP monolayer was analyzed at a surface pressure of $\pi = 30$ mN/m using a home-made Teflon trough of dimensions 70 mm \times 70 mm \times 4 mm covered by a lid to prevent evaporation. The DMPC-DMPG SUVs were injected with a syringe directly into the subphase through a thin side channel. The ratio of the complex reflection coefficients for p -polarized and s -polarized light, r_p and r_s , can be described by the two ellipsometric angles Ψ and Δ ²⁰:

$$\frac{r_p}{r_s} = \tan \Psi e^{-i\Delta} \quad (1)$$

These two angles depend on the refractive indices of the two bulk media and the refractive index and thickness of the lipid film. Within the framework of a specific layer model (software Elli70 by Optrel) and with fixed refractive indices for all components, the lipid layer thickness can thus be reconstructed from the measurements²¹.

2.4. X-ray Reflectometry (XRR)

XRR measurements were performed using a D8 Advance reflectometer (Bruker AXS, Karlsruhe, Germany) featuring a vertical goniometer and horizontal sample geometry, allowing the liquid surface to be studied without being disturbed during the measurements. A Langmuir trough (KSV 1000, Helsinki, Finland) with one Teflon barrier for asymmetric film compression was enclosed in a box with Kapton windows through which the incident and reflected X-ray beams pass. The dimensions of the trough were 85 mm \times 320 mm \times 4 mm for a total subphase volume of ≈ 110 mL when filled to a positive meniscus.

Reflectivity curves were measured in the $\theta - 2\theta$ geometry, where θ is the incident angle. A conventional X-ray tube with a Cu anode (Cu K_α , wavelength $\lambda = 1.54$ Å) was used to generate an X-ray beam with a line focus. The beam was monochromized by a Göbel mirror (W/Si multilayer mirror) and collimated through two narrow horizontal slits of 0.1 mm with a switchable absorber (calibrated Cu

attenuator) in between. Soller slits ($\Delta\theta_x = 25$ mrad) were placed after the last horizontal slit and directly in front of the detector. The intensity was recorded with a Vântec-1 line detector (Bruker AXS, Germany). Data were corrected using the known attenuation factors. Finally, the angular reflectivity scans were transformed to reflectivity curves as a function of the perpendicular scattering vector component, $Q_z = 4\pi \sin \theta / \lambda$ ²². For analysis, the experimental data were compared with theoretically modeled XRR curves based on a slab-model representation of the electron density profiles of the interfacial lipid layers. These profiles were discretized into 1-Å-thin sub-slabs of constant electron density, and the corresponding Q_z -dependent reflectivities, $R(Q_z)$, were then calculated from the Fresnel reflection laws at each slab-slab interface using the iterative recipe of Parratt²³. Finally, all model parameters (electron densities, layer thicknesses, and roughness) were varied until the best agreement with the experimental data was reached via χ^2 minimization.

2.5. Grazing-incidence X-ray scattering techniques

Grazing-incidence X-ray scattering experiments (GIXOS, GIXD, and TRXF, see below) were carried out at the beamline P08 at storage ring PETRA III of Deutsches Elektronen-Synchrotron (DESY, Hamburg, Germany). The Langmuir trough (Riegler & Kirstein, Potsdam, Germany) was located in a hermetically sealed container with Kapton windows, and the temperature was kept at 27°C by a thermostat. The container was constantly flushed with a stream of humidified helium (He) to prevent air scattering and the generation of reactive oxygen species. The synchrotron X-ray beam was monochromatized to a photon energy of 15 keV, corresponding to a wavelength of $\lambda = 0.827$ Å. The incident angle was adjusted to $\theta_i = 0.07^\circ$, slightly below the critical angle of total reflection, $\theta_c = 0.082^\circ$. A ground glass plate was placed approximately 1 mm beneath the illuminated area of the monolayer in order to reduce mechanically excited surface waves.

Under total-reflection conditions an X-ray standing wave (SW) is formed at the air/water interface. The penetration depth of its evanescent tail into the aqueous hemisphere is a function of the angle of incidence θ_i ²⁴:

$$\Lambda \cong \frac{1}{Q_c} \sqrt{\frac{\theta_c^2}{\theta_c^2 - \theta_i^2}} \quad (2)$$

where $Q_c = 4\pi \sin \theta_c / \lambda$ is the momentum transfer at the critical angle, such that $\Lambda \approx 8$ nm. The exact shape $\Phi(z)$ of the SW intensity along the vertical position z for a given incident angle follows from the interfacial electron density profile $\rho(z)$ and can be computed via the phase-correct summation of all reflected and transmitted partial waves occurring at the density gradients, as has been described previously^{25, 26}. For lipid layers immobilized at the air/water interface, the profile $\rho(z)$ can be described conveniently with a slab model²⁷, where the parameters of individual slabs in terms of thickness, electron density, and roughness can be obtained by XRR²⁸⁻³⁰ or GIXOS³¹⁻³³, see further below. Note that roughness can be neglected for the computation of $\Phi(z)$ when Q_z is low, as is the case under total reflection²⁷.

2.5.1. Grazing incidence X-ray off-specular scattering (GIXOS)

Analogous to conventional X-ray reflectometry, GIXOS allows reconstructing the interfacial electron density profile (i.e., the laterally-averaged structure of the surfactant layer in the direction perpendicular to the surface) from the Q_z -dependent scattering intensity, however at fixed incident angle. The details of this technique are described elsewhere^{30, 34, 35}. As explained more briefly in Kanduč et al.³⁶, the Q_z -dependence of the diffuse scattering intensity $I(Q_{xy} \neq 0, Q_z)$ recorded at low-enough yet finite Q_{xy} (“out of the specular plane”) with the help of a narrow slit contains information equivalent to that of the conventional reflectivity $R(Q_z)$ and can be transformed as $I(Q_{xy} \neq 0, Q_z) = V(Q_z) R(Q_z) / R_F(Q_z)$ to good approximation, where $V(Q_z)$ is the Vineyard function and $R_F(Q_z)$ the Fresnel reflectivity of an ideal surface between the two bulk media. The approximation is based on the assumption of conformal topographic roughness of all surfaces, which is justified for molecular surface layers subject to capillary wave roughness. In the present work, the GIXOS signal was measured at $Q_{xy} = 0.04 \text{ \AA}^{-1}$. The experimental data were analyzed with slab models as described above for XRR, but in this case the calculated reflectivities $R(Q_z)$ were multiplied with $V(Q_z) / R_F(Q_z)$ to obtain the theoretical GIXOS signal.

2.5.2. Grazing incidence X-ray diffraction (GIXD)

The diffraction signal was measured with a vertically-oriented position-sensitive detector (PSD, Mythen2 1K, Dectris AG, Baden-Daettwil, Switzerland) scanning the azimuthal angle Δ and, with that, the in-plane component $Q_{xy} = 4\pi/\lambda \sin(\Delta/2)$ of the scattering vector Q . The in-plane divergence of the diffracted beam was restricted to 0.09° with a Soller collimator (JJ X-ray, Denmark). The out-of-plane component Q_z of the scattering vector is encoded in the vertical position of the PSD channels and covered the range from 0.0 to 1.2 \AA^{-1} . The diffraction data consist of Bragg peaks in the 2-dimensional (Q_{xy}/Q_z) space. The diffraction peaks were fitted with a self-written python macro yielding their Q_{xy} and Q_z positions and the full width at half maximum (FWHM, see ³⁷ for the details). The in-plane lattice repeat distances t of the ordered structures then follow from Bragg's law as $t = 2\pi/Q_{xy}$. The lattice parameters such as the chain tilt with respect to the vertical direction and the cross-sectional area per chain were obtained from the peaks' Q_{xy} and Q_z positions as described elsewhere ³⁷⁻³⁹.

2.5.3. Total-reflection X-ray fluorescence (TRXF)

The fluorescence signal induced via photoelectric ionization by the X-ray beam under total reflection conditions was recorded with an Amptek X-123SDD detector (Amptek, Bedford, USA). The detector was placed almost parallel to the water surface and perpendicular to the X-ray beam axis, in order to keep elastic and Compton scattering into the detector as low as possible. The center of the detector view angle was set to coincide with the beam footprint position on the water surface.

The fluorescence intensity I_P emitted by the phosphorus (P) atoms contained in the interfacial lipid layer is determined by their interfacial depth profile $c_P(z)$ ²⁷. On a quantitative level, I_P is proportional to the spatial integral over the product of $c_P(z)$ and the known SW intensity profile $\Phi(z)$ introduced above,

$$I_P = A \int_{-\infty}^{\infty} c_P(z) \Phi(z) dz \quad (3)$$

where the prefactor A can be calibrated with a suitable reference measurement for which $c_P(z)$ is known. Experimentally, I_P was obtained by fitting the intensity

peak associated with the $P K_\alpha$ emission line (at ≈ 2.05 keV) in the recorded fluorescence spectra with a Gaussian function.

2.5.4. Determination of the DMPC-DMPG bilayer coverage by TXRF

The P fluorescence intensity after bilayer adsorption was interpreted on a quantitative level by considering the initial intensity originating solely from the P atoms in the DPPE-DSTAP monolayer. Their in-plane density Γ_P^m is determined by the GIXD measurements, yielding the area per lipid in the monolayer $A_L^m = 41.2 \text{ \AA}^2$ (see section 3.1.1) and thus the P -coverage in the monolayer,

$$\Gamma_P^m = f_P^m / A_L^m \quad (4)$$

where $f_P^m = 0.7$ is the fraction of lipids carrying a P atom. The depth distribution of P along z can be well approximated with a narrow region of extension l analogous to the headgroup slab of the monolayer, such that the P concentration in this region is $c_P^m = \Gamma_P^m / l$. With that, $c_P(z)$ is fully determined and, together with the known SW intensity profile Φ , yields an absolute calibration of the prefactor A in Eq. 3. It should be noted however that the precise value of l has negligible influence on the final result.

After adsorption of the DMPC-DMPG bilayer, two additional P -accommodating regions are considered, coinciding with the phospholipid headgroup slabs at the two bilayer surfaces. The P coverage in each of these regions is determined by the coverage fraction x_b (see Results section) and the average lipid area $A_L^b = 59.9 \text{ \AA}^2$ in a DMPC-DMPG bilayer in the L_α phase ⁴⁰,

$$\Gamma_P^b = x_b f_P^b / A_L^b \quad (5)$$

, where $f_P^b = 1$ because every lipid carries a P atom. The coverage fraction can thus be expressed in terms of the ratio between the coverages of P atoms in the monolayer and bilayer surfaces.

$$x_b = f_P^m \frac{A_L^b \Gamma_P^b}{A_L^m \Gamma_P^m} \cong 0.92 \cdot \frac{\Gamma_P^b}{\Gamma_P^m} \quad (6)$$

This coverage ratio, in turn, can be deduced from the ratio I_P/I_P^0 between the measured fluorescence intensities before and after bilayer adsorption (see section 3.1.4).

2.5.5 Determination of the DMPC-DMTAP bilayer coverage by TXRF

The coverage of a DMPC-DMTAP bilayer adsorbed to a PFOL-PFOA monolayer was determined in the same way, but with a suitably adapted slab model which considers that the perfluorinated monolayer is *P*-free. As a *P*-containing calibration reference, the DPPE-DSTAP monolayer was again used.

3. Results and Discussion

3.1. DMPC-DMPG bilayer supported by a DPPE-DSTAP monolayer

The preparation of conventional floating lipid bilayers¹⁵ is typically based on the Langmuir-Blodgett (LB) and/or Langmuir Schaefer (LS) techniques^{9, 41}. This approach obviously cannot be taken for the deposition of lipid bilayers onto fluid interfaces and the vesicle fusion technique^{42, 43} has to be employed instead. Although its effectiveness depends on many parameters, notably on a suitable functionalization of the interface, vesicle fusion has an overall greater potential to be used also for native membrane systems⁴⁴.

As in the case of solid-supported floating bilayers, a phospholipid surface is initially used as support for the bilayer deposition in the present work. For this purpose, a monolayer of DPPE-DSTAP (70:30 mol%) was chosen. The zwitterionic phospholipid DPPE has fully saturated C16 hydrocarbon chains and adopts a liquid-condensed (LC) state at 27°C⁴⁵, the temperature at which this study was carried out. In order to promote the fusion of negatively charged vesicles we added to the monolayer 30 mol% of the positively charged lipid DSTAP, which has fully saturated C18 hydrocarbon chains and also forms a considerably rigid film⁴⁶. The lipids were spread onto an air-water interface from a chloroform-methanol (7:3 v/v) solution and then compressed until reaching a final lateral pressure of $\pi = 30$ mN/m, a representative value of the packing in lipid bilayers⁴⁷. Fig. 1 shows compression isotherms for the monolayers of the different lipidic mixtures employed during this work. The isotherm of the DPPE-DSTAP monolayer (red solid line) shows that the film transitions into an ordered LC phase already at very low pressures and is very stable up to $\pi = 55$ mN/m. Our purpose was to study bilayers in a fluid-like L_α phase. Therefore, the choice of a monolayer in an ordered LC phase was intended to avoid undesired lipid exchange between the adjacent mono- and bilayers. The SUVs for vesicle fusion were prepared using a 70:30 mol% mixture of DMPC and DMPG, a system that is negatively charged and assumes a fluid L_α phase at 27°C, the temperature at which the measurements were conducted. The SUVs were slowly injected into the subphase under the pre-formed monolayer film ($\pi = 30$ mN/m) with a syringe

and from the opposite side of the compression barriers until reaching a final lipid concentration of 0.1 mg/ml in the subphase.

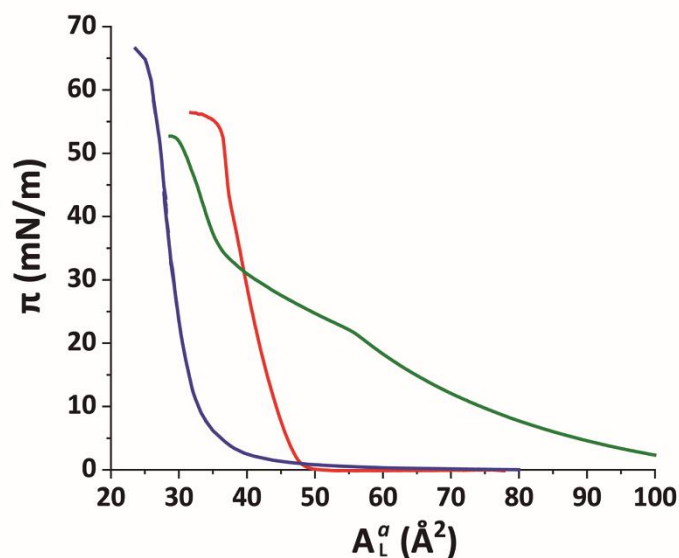


Fig. 1: Compression isotherms (lateral pressure π vs. available area per molecule A_L^a) for DPPE-DSTAP (red), PFOL-PFOA (blue) and DMPC-DMTAP (green) mixed monolayers at 27°C. A_L^a was calibrated with the crystallographic area A_L^c for each mixture at $\pi = 30$ mN/m (DPPE-DSTAP: $A_L^c = 41.2$ Å²; PFOL-PFOA: $A_L^c = 29.1$ Å²; DMPC-DMTAP: $A_L^c = 44.6$ Å²).

3.1.1. In-plane structure of the DPPE-DSTAP monolayer: GIXD

To obtain information on the in-plane lattice structure of the DPPE-DSTAP monolayer, GIXD experiments were performed. The GIXD pattern obtained at $\pi = 30$ mN/m is shown in Fig. S1 in the Supporting Information. Two distinct Bragg peaks indicate the formation of a rectangular lattice structure with tilted chains (tilt angle 14.5°) in the nearest neighbor (NN) direction³⁸. The crystallographic area per lipid, $A_L^c = A_L^m = 41.2$ Å², demonstrates tight lipid packing. The chain cross-sectional area ($A_0 = 20.0$ Å²) is typical of a free rotator phase³⁸.

3.1.2. Bilayer formation kinetics: ellipsometry

Ellipsometry was used to monitor the total lipid layer thickness D (monolayer + bilayer) as a function of time after the injection of DMPC-DMPG SUVs. The thickness was deduced from the ellipsometric angles (see section 2.3) with an

assumed refractive index for lipids, $n = 1.46$, which is an approximate mean value between the reported refractive indices of DPPE⁴⁸ and DMPC⁴⁹. For air and water, refractive indices of 1.00 and 1.33 were assumed. Fig. 2 shows the evolution of the total thickness D . The initial thickness corresponding to the monolayer is obtained as 2.6 nm, which meets the expectation for a monolayer well. Upon vesicle fusion, D increases gradually until it saturated to a value of 7.3 nm after about 8 h. The difference between the final and initial values, $\Delta D = 4.7$ nm, is a reasonable value for the thickness of a fluid bilayer containing DMPC⁵⁰. The intermediate thickness values obtained during the bilayer formation process can be understood in terms of a gradually increasing bilayer coverage fraction until full coverage is reached eventually.

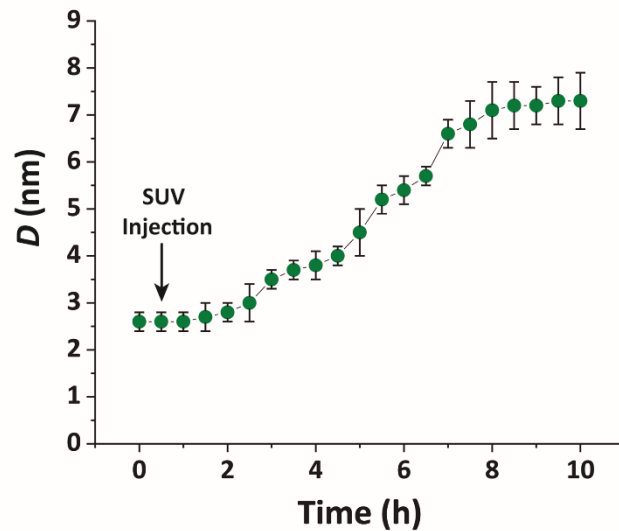


Fig. 2: Total lipid layer thickness D obtained by ellipsometry as a function of time after the injection of DMPC-DMPG SUVs underneath a pre-formed DPPE-DSTAP monolayer at $\pi = 30$ mN/m. The error bars correspond to the standard deviation of 4 independent experiments.

3.1.3. Vertical sample structure: GIXOS and XRR

GIXOS and XRR experiments were carried out to determine the interfacial layer structures in terms of the interfacial electron density profiles. Fig. 3A presents the GIXOS curve for the DPPE-DSTAP monolayer at $\pi = 30$ mN/m. The data were analyzed by describing the monolayer film with two homogeneous slabs or boxes of adjustable thickness d and electron density ρ , which physically represent different portions of the lipid monolayers, namely headgroups and hydrocarbon

tails. The interfaces between slabs are subject to interfacial roughness to an
 adjustable extent encoded in the roughness parameters σ . In Fig. 3A, the solid
 red line superimposed to the experimental data points is a theoretically modeled
 GIXOS signal based on such a two-layer description after optimization of the
 parameters d and ρ of both slabs and of the σ parameters for the three interfaces.
 The associated best-matching electron density profile is shown in Fig. 3B. The
 first layer has a comparatively low electron density and represents the tails of the
 monolayer (“tm”), while the second layer has a higher electron density and
 represents the headgroups of the monolayer (“hm”). The best-matching
 parameters are summarized in Table 1 and are similar to those reported earlier
 for a pure DPPE monolayer⁴⁸. The provided error estimates include systematic
 uncertainties, which are typically the dominant contribution as discussed
 previously⁵¹.
 Note that the electron density in the headgroup is somewhat lower than in usual
 phospholipid layers, because here 30% of the lipids (DSTAP) do not have
 electron-rich *P* atoms in their headgroups. The comparatively high electron
 density of the tail layer is consistent with the reported structures of densely
 packed monolayers of lipids with saturated tails⁵². The obtained roughness
 values are comparatively low, which can be attributed to the fact that GIXOS
 measures the scattering signal at finite Q_{xy} ⁵³.

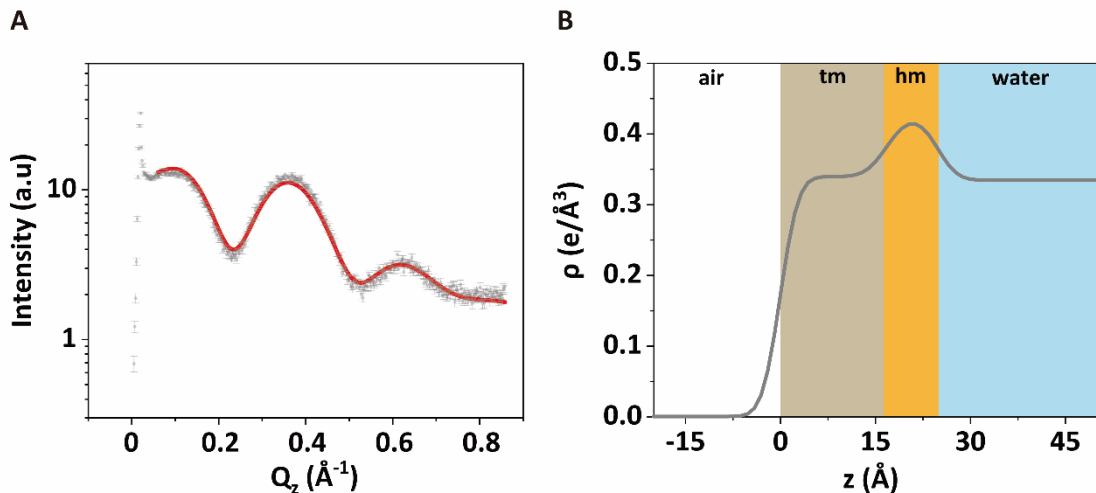


Fig. 3: (A) GIXOS signal (symbols) from a DPPE-DSTAP monolayer at $\pi = 30$
 mN/m. The solid red line is the theoretical curve corresponding to the best-
 matching model parameters. (B) Reconstructed electron density profile of the
 monolayer at the air/water interface. The colored regions labeled with “tm” and
 “hm” represent the tail and headgroup sections of the monolayer.

	d (Å)	ρ (e/Å ³)	σ (Å)	
hm	8.1 ± 0.5	0.42 ± 0.01	σ_1 (air/tm)	2.2 ± 0.5
tm	16.8 ± 0.5	0.34 ± 0.01	σ_2 (tm/hm)	2.6 ± 0.5
			σ_3 (hm/water)	2.4 ± 0.5

Table 1: Parameters of the best-matching model for a DPPE-DSTAP monolayer at $\pi = 30$ mN/m as obtained by GIXOS. The labels “hm” and “tm” stand for monolayer headgroups and monolayer tails, respectively. Error estimates include systematic uncertainties.

Fig. 4A shows the GIXOS curve measured 6 h after the injection of DMPC-DMPG SUVs underneath the DPPE-DSTAP monolayer. The solid line indicates the theoretical curve corresponding to the best-matching parameters of the slab model. This time, a more complex slab model was used to describe a bilayer adsorbed underneath the monolayer. In addition to the “tm” and “hm” slabs introduced before, slabs for the headgroups, tails, and the central methyl dip of the bilayer (“hb”, “tb”, and “mb”, respectively) as well as a water layer “w” between monolayer and bilayer were considered. Note that the “hb” and “tb” layers appear twice in the bilayer for reason of symmetry (see Fig. 4 B). In order to minimize the number of free parameters in the model, the monolayer-related features were kept at the values obtained prior to vesicle fusion (Table 1). All bilayer-internal parameters were fixed such that they exactly reproduced (see Fig. S2 in SI) a previously published electron density profile of a DMPC bilayer in the fluid L_α phase⁵⁴. These fixed bilayer values are presented in Table 2. However, in order to realistically model an imperfect, fluctuating bilayer adsorbed to a monolayer, we further considered a global bilayer roughness, achieved by convolution of the bilayer profile with a Gaussian function of width σ_{conv} (see Table 3, 1st column). This was achieved analytically by correcting all bilayer-related slab roughness parameters as $\sigma_{\text{corr}} = \sqrt{\sigma^2 + \sigma_{\text{conv}}^2}$. Moreover, we allowed for scenarios of incomplete bilayer coverage by introducing the coverage fraction $x_b \in [0, 1]$. The latter was implemented through weighted averaging of the electron density profile of the bilayer (with weight x_b) and of the constant electron density of water (with weight $1 - x_b$). The remaining free model parameters to fit the GIXOS intensity curve in Fig. 4A are only the thickness d_w of the interstitial water layer, the global bilayer roughness σ_{conv} , and the bilayer coverage fraction x_b .

The good agreement between the theoretical GIXOS curve and the experimental data demonstrates the validity of the employed model upon optimization of these three parameters. In this case, the overall architecture of the trilayer can be roughly described as a 5 nm thick bilayer floating at a separation of ≈ 1 nm below a 2.5 nm thick monolayer, which is in good agreement with the ellipsometry results discussed before.

The main obstacle to an unambiguous determination of the parameter values is a strong covariance between σ_{conv} and x_b in the fit. Namely, a theoretical GIXOS or XRR curve undergoes similar changes when increasing x_b or when decreasing σ_{conv} ^a. This undesirable ambiguity can however be circumvented through an independent determination of x_b by TXRF measurements, as explained in section 2.5.4.

An equivalent experiment on a monolayer/bilayer system of the same composition was performed by XRR with the same model-based analysis procedure. The XRR fitting curve (Fig. S3 and table S1 in SI), like the GIXOS curve, is well reproduced by the model and the sample is clearly found to have the expected trilayer architecture. In fact, the agreement is satisfactory even when modelling the XRR experimental data with the model parameters found for in the GIXOS measurements (see again Fig. S3 in SI). While the main structural characteristics obtained by GIXOS and XRR are generally consistent, eventual differences can be attributed to the different roughness bias of the two techniques⁵³ but also to the coverages that can be slightly different in two different experiments.

	d (Å)	ρ (e/Å ³)		σ (Å)
hm	8.1	0.42	σ_1 (air/tm)	2.2
tm	16.8	0.34	σ_2 (tm/hm)	2.6
hb	6.7	0.50	σ_3 (hm/water)	2.4
tb	10.9	0.30	σ_4 (water/hb)	1.8
mb	7.0	0.17	σ_5 (hb/tb)	2.4
			σ_6 (tb/mb)	2.4

^a This is the case for X-rays, because bilayers on average have similar ρ as water and contrast therefore mainly arises from bilayer internal ρ variations which vanish when getting smeared out by convolution. For neutrons, the situation is different.

Table 2: Fixed parameters used for the GIXOS, XRR and TXRF fittings of the trilayer architecture formed by a DPPE-DSTAP monolayer and DMPC-DMPG bilayers. The monolayer parameters were extracted from the fitting of Fig. 3, and the bilayer parameters were taken from the bibliography ⁵⁴.

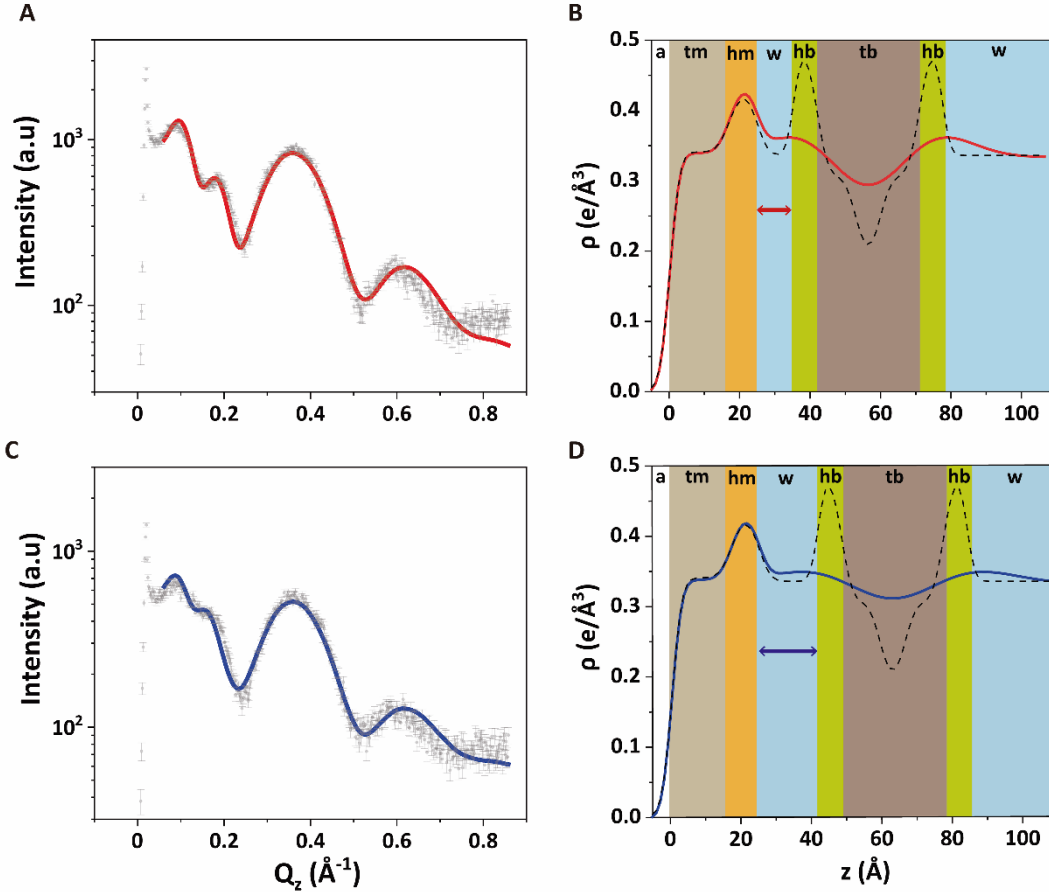


Fig. 4: (A, C) GIXOS data (symbols) and the corresponding fits (solid lines) for the trilayer system (DPPE-DSTAP monolayer + adsorbed DMPC-DMPG bilayer) 6 hours after SUVs injection (A) without and (C) with added NaCl. (B, D) Reconstructed electron density profiles (solid lines) for the trilayer (B) without and (D) with added NaCl. The different colors represent the sections with different electron density values. The plots with dashed lines represent non-convolved electron density profiles, when setting $\sigma_{\text{conv}} = 0$ \AA . All profiles represent the regions covered by a bilayer, i.e., for $x_b = 1$.

3.1.4. Bilayer coverage fraction: TRXF

TRXF experiments were carried out simultaneously with GIXOS and GIXD, in order to quantify the bilayer coverage fraction x_b introduced above. Since this fraction is proportional to the interfacial density of P atoms belonging to the bilayer, it is possible to deduce x_b from measurements of the P fluorescence intensity I_P . Fig. 5A shows this intensity as a function of time after injection of

DMPC-DMPG SUVs underneath the DPPE-DSTAP monolayer. The intensity is normalized by its value I_p^0 prior to SUVs injection. After injection the intensity increases systematically as the bilayer is formed and reaches a value of $I_p/I_p^0 = 1.77$ at the end of the measurement after 6h, when GIXOS was measured. Note that the intensity has not yet saturated at that point.

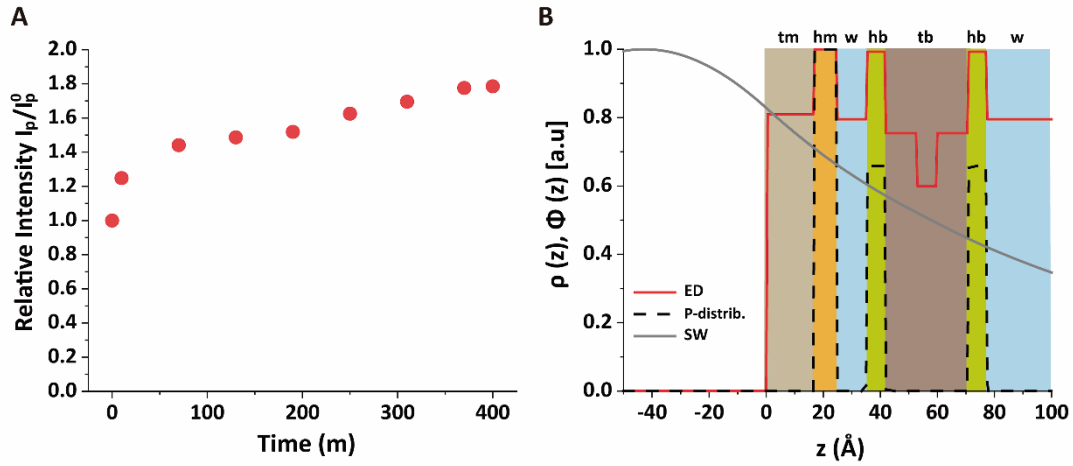


Fig. 5: (A) Relative intensity I_p/I_p^0 as a function of time after SUVs injection. (B) Schematic illustration of the lipid layers with a slab description of the electron density profiles (red solid line), P distributions (black dashed line) and calculated SW X-ray intensity (grey solid line).

As described in the Methods section, the bilayer coverage was deduced from the increase in the P fluorescence based on the interfacial SW profile and the distribution of P atoms. Fig. 5B shows the structure of the air/water interface after the bilayer adsorption in terms of the electron density slab model and the P distribution. The grey solid line indicates the SW intensity profile at the relevant incidence angle, which was found to be practically identical before and after bilayer adsorption. The profile was calculated with the monolayer and bilayer parameters summarized in Tables 1 and 2⁵⁴. Importantly, the SW intensity is higher at the monolayer surface than at the bilayer surfaces, which is why the bilayer contributes less to the P fluorescence intensity than the monolayer. Rigorous application of Eq. 3 for both scenarios reproduces the observed intensity ratio $I_p/I_p^0 = 1.77$ when $\Gamma_P^b/\Gamma_P^m = 0.54$, such that the coverage fraction is obtained as $x_b = 0.50$ according to Eq. 6.

In other words, no full bilayer coverage was achieved after 6h, which is consistent with the non-saturated P intensity in Fig. 5A and with the ellipsometry results which show that full coverage can take more than 8h. By analyzing the ellipsometry results (Fig. 2), it can even be seen that the apparent bilayer thickness 6 hours after the vesicle injection represents a 59% fraction of the final stable bilayer thickness after 8 hours, in satisfactory agreement with the value $x_b = 0.50$ obtained by TRXF.

3.1.5. Final structural modeling and the effect of added salt

With x_b at hand, a final fitting of the GIXOS data on the DMPC-DMPG bilayer supported by the DPPE-DSTAP-functionalized air/water interface was performed. By fixing all the structural parameters summarized in the Table 2 as well as $x_b = 0.50$, reliable values for the water layer thickness and the global roughness were obtained (Table 3). The solid line in Fig. 4A corresponds to this final fit result, and the corresponding electron density profile is shown in Fig. 4B as a solid line. For better illustration this profile represents the regions effectively covered by a bilayer, i.e., when assuming $x_b = 1$.

The water layer thickness d_w was found to be around 10 Å, in line with the picture that hydration repulsion prevents a direct surface contact despite the electrostatic attraction⁵⁵. With $\sigma_{\text{conv}} \approx 10$ Å, the global bilayer roughness was found to be larger than that of conventional solid-supported lipid bilayers and comparable to that of floating lipid bilayers¹⁵, reflecting the soft overall bilayer confinement at the functionalized air/water interface. To illustrate the influence of bilayer roughness, the non-convolved electron density profile (i.e., when assuming $\sigma_{\text{conv}} = 0$ Å) is also shown in Fig. 4B as a dashed line.

We further investigated the electrostatic effect of salt addition on the interaction of the DMPC-DMPG bilayer with the supporting DPPE-DSTAP monolayer. For this purpose, NaCl was added to a final concentration of 50 mM and another GIXOS measurement was carried out only 15 min later. The most remarkable effect caused by the salt addition is a water layer thickening (Table 3 and Fig. 4C-D) by around 7 Å (from $d_w \approx 10$ Å to $d_w \approx 17$ Å) which could be explained due to the screening of ions and the resulting weaker attraction between the oppositely charged layers. In fact a similar value of $d_w \approx 20$ Å has been previously reported

for the separation between uncharged DPPC bilayers at full hydration ⁵⁶, suggesting that hydration repulsion becomes the dominant short-range force contribution for sufficiently high ionic strength. The weaker adhesion strength in the presence of salt appears to correlate also with an increase in the bilayer roughness (see Table 3), as was previously discussed for solid-supported floating bilayers ¹⁵.

	Trilayer	Trilayer + salt
x_b	0.50 ^a	0.50 ^a
d_w (Å)	10.3 ± 0.5	16.6 ± 0.5
σ_{conv} (Å)	10.2 ± 0.5	13.3 ± 0.5

Table 3: Parameters of the best GIXOS matching model for the trilayer system (DPPE-DSTAP monolayer + DMPC-DMPG vesicles) 6 hours after SUVs injection with and without NaCl. ^aKnown from TXRF measurement and therefore fixed. Error estimates include systematic uncertainties.

3.2. DMPC-DMTAP bilayer supported by a PFOL-PFOA monolayer

The combination of GIXOS, TXRF, and ellipsometry allowed us to characterize the vertical sample architecture, i.e., perpendicular to the interface. In contrast, GIXD allows for the investigation of lipid layers in the in-plane direction and can resolve the details of the molecular arrangements in lipid phases with crystalline ordering ^{37, 39}. The technique is largely limited to air/water interfaces and has therefore been used almost exclusively for the study of lipid monolayers ^{52, 57}. However, having at hand lipid bilayers immobilized at air/water interfaces, we are in the unique position to exploit the power of GIXD for the study of lipid bilayers featuring phases with crystalline ordering, such as the chain-ordered L_β phase.

In order to distinguish the diffraction peaks from the monolayer and the bilayer, any overlap between the associated peak positions should be avoided, which is difficult when the monolayer is formed by conventional membrane lipids able to form ordered LC phases. To overcome this issue, a second experiment was performed in which the air/water interface was functionalized with a negatively charged monolayer formed by the perfluorinated amphiphiles 1H,1H-Perfluorooctadecan-1-ol (PFOL) and Perfluorooctadecanoic acid (PFOA), also in the molar proportion 70:30. The PFOL-PFOA isotherm (Fig. 1, blue solid line) was found to be featureless, steep, and stable up to $\pi = 65$ mN/m, indicating

densely arranged perfluorocarbon chain domains at all conditions. The SUVs were prepared from a positively charged mixture of DMPC-DMTAP (70:30 mol %). At 27°C, an ordered L_β structure is expected for this mixture, for which an L_β to L_α phase transition temperature of $\approx 36^\circ\text{C}$ was reported by Zantl et al ⁵⁸.

The GIXOS curves of the compressed PFOL-PFOA monolayer ($\pi = 30$ mN/m) prior to and after the injection of DMPC-DMTAP SUVs, clearly reveal the formation of a bilayer adsorbed to the monolayer (Fig. 6 A and B). The fluorinated molecules of the monomolecular film were described as a single slab (labeled as “f”) with an adjusted thickness $d_f \approx 21$ Å and an electron density $\rho = 0.66$ e/Å³ (Table 4) which agree well with those previously reported by Sperati ⁵⁹ and by Jacquemain ⁶⁰ for similar fluorinated compounds. The DMPC-DMTAP bilayer was modeled in the same way as the DMPC-DMPG bilayer discussed above, based on reference ⁵⁴. Based on $x_b = 0.55$, obtained by TRXF (see Methods section), the best-matching values for the two remaining parameters were obtained as $d_w \approx 5$ Å and $\sigma_{\text{conv}} < 2$ Å (see also Table 4). As can be seen, the interstitial water layer is significantly thinner than that of the DPPE-DSTAP-DMPC-DMPG system, which can be explained due to a much weaker hydration repulsion. In fact, it has been already reported that hydration repulsion is of much longer range for zwitterionic phospholipid surfaces than for surfaces bearing OH-groups ⁶¹. Besides, a stronger charge attraction can be attributed to a higher charge density in the monolayer. Regarding σ_{conv} we can assume that its remarkably low value is likely a consequence of the stronger adhesion and the overall higher rigidity of the perfluorinated monolayer.

Fig. 7A shows the GIXD pattern of the PFOL-PFOA monolayer prior to injection of DMPC-DMTAP SUVs. It exhibits a single sharp diffraction peak with the maximum at $Q_z = 0$, indicating that the fluorocarbon chains assume an upright (un-tilted) hexagonal lattice. From the peak position $Q_{xy} = 1.268$ Å⁻¹ (Fig 7A, inset), the corresponding lattice spacing between fluorocarbon chains of 5.72 Å can be calculated, which agrees well with the value reported earlier ⁶². Also for the shorter perfluorododecanoic acid (C11F23COOH) the same non-tilted phase has been observed between 15 and 50 mN/m with lattice-spacings decreasing from 5.83 Å to 5.77 Å on compression ⁶³.

	d (Å)	ρ (e/Å ³)
f	21.4 ± 0.5	0.66 ± 0.01
d_w (Å)		4.9 ± 0.5
σ_{conv} (Å)		1.3 ± 0.5
x_b		0.55^a
σ_1 (air/f)		3.2 ± 0.5
σ_2 (f/water)		1.8 ± 0.5

Table 4: Parameters of the best GIXOS matching model for the trilayer system (PFOL-PFOA monolayer + DMPC-DMTAP vesicles) 6 hours after the vesicles spreading. The superscript ^a refers to those values fixed prior to the fitting, in this case from TXRF. The DMPC-DMTAP bilayer was modeled in the same way as the DMPC-DMPG bilayer discussed above, based on reference ⁵⁴. Error estimates include systematic uncertainties.

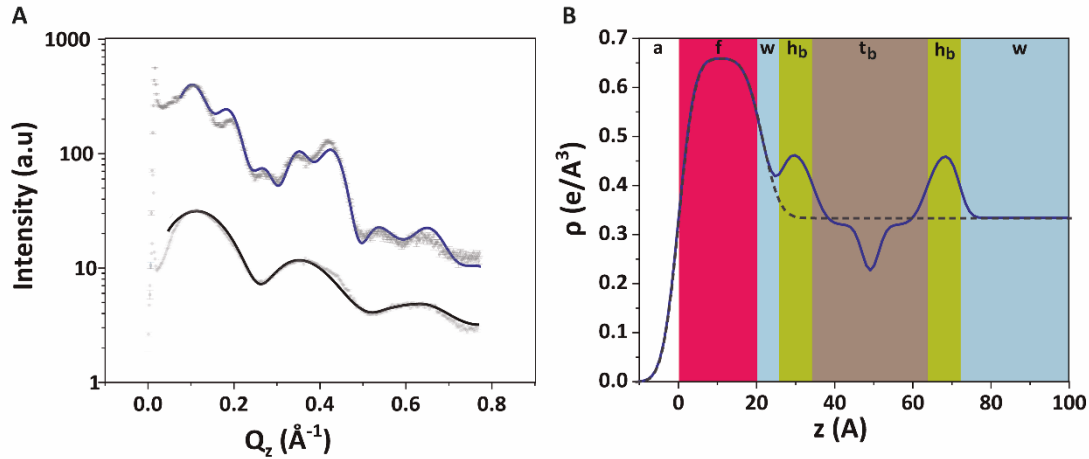


Fig. 6: (A) GIXOS data (symbols) and the corresponding fits (solid lines) for the PFOL-PFOA (70:30 mol %) monolayer at $\pi = 30$ mN/m (black) and 6h after injection of DMPC-DMTAP SUVs (blue). (B) Reconstructed electron density profile for the monolayer (dashed line) and the trilayer (solid line). The different colours represent the sections with different electron density values. All profiles represent the regions covered by a bilayer, i.e., for $x_b = 1$.

The GIXD pattern recorded 6 hours after the injection of DMPC/DMTAP SUVs features additional diffraction intensity around $Q_{xy} = 1.49$ Å⁻¹, which can safely be attributed to the formed bilayer (Fig. 7B). The first impression is that this additional intensity is from a single diffraction peak centered at $Q_z \approx 0$, which would indicate a fully upright hexagonal packing of the lipid tails in the bilayer. However, the width of the peak in Q_z -direction (FWHM = 0.41 Å⁻¹) according to the Scherrer equation^{24, 37} corresponds to an alkyl chain layer thickness of only

14 Å, which is clearly too thin for a layer of stretched upright C14 tails. When a realistic value of $L = 17$ Å (corresponding to FWHM = 0.34 Å⁻¹) is imposed in a suitable model with two closely overlapping peaks, then fitting yields $Q_{xy1} = 1.485$ Å⁻¹, $Q_{xy2} = 1.494$ Å⁻¹, $Q_{z1} = 0.12$ Å⁻¹ and $Q_{z2} = 0$ Å⁻¹ (see Fig. 7C and D), which corresponds to a chain tilt of $\approx 5.3^\circ$ and area per molecule of $A_L^b = 41.2$ Å². Note that in the work by Zantl et al. on the same lipid composition⁵⁸, the single intensity maximum observed in wide-angle X-ray scattering (WAXS) at $Q_{xy} \approx 1.48$ Å⁻¹ has also been interpreted as a superposition by powder averaging of the two separate peaks associated with a tilted chain lattice.

In contrast, in the monolayer of the DMPC-DMTAP (70:30 mol %) mixture, for which the isotherm is also shown in Fig. 1 (green solid line), three diffraction peaks are observed at high lateral pressures (see Fig. S4 in SI). They correspond to an LC phase with a crystallographic area per molecule of $A_L^m = 44.6$ Å² and a chain tilt angle of $\alpha = 21.8^\circ$. Interestingly, the bilayer behaves differently than the monolayer of the same mixture, for which the tilt is much larger. As was already pointed out earlier, this result demonstrates the usefulness of GIXD experiments on lipid bilayers immobilized at air/water interfaces, as they allow for the investigation of bilayer structures that do not necessarily occur in the corresponding monolayers¹⁹.

Upon bilayer formation, also a slight lateral contraction in the fluorinated monolayer structure occurs, as manifested in a shift in the diffraction peak from $Q_{xy} = 1.268$ Å⁻¹ to $Q_{xy} = 1.273$ Å⁻¹. This molecular area decrease by roughly 1% could be related to an effective charge screening by the presence of the oppositely charged bilayer.

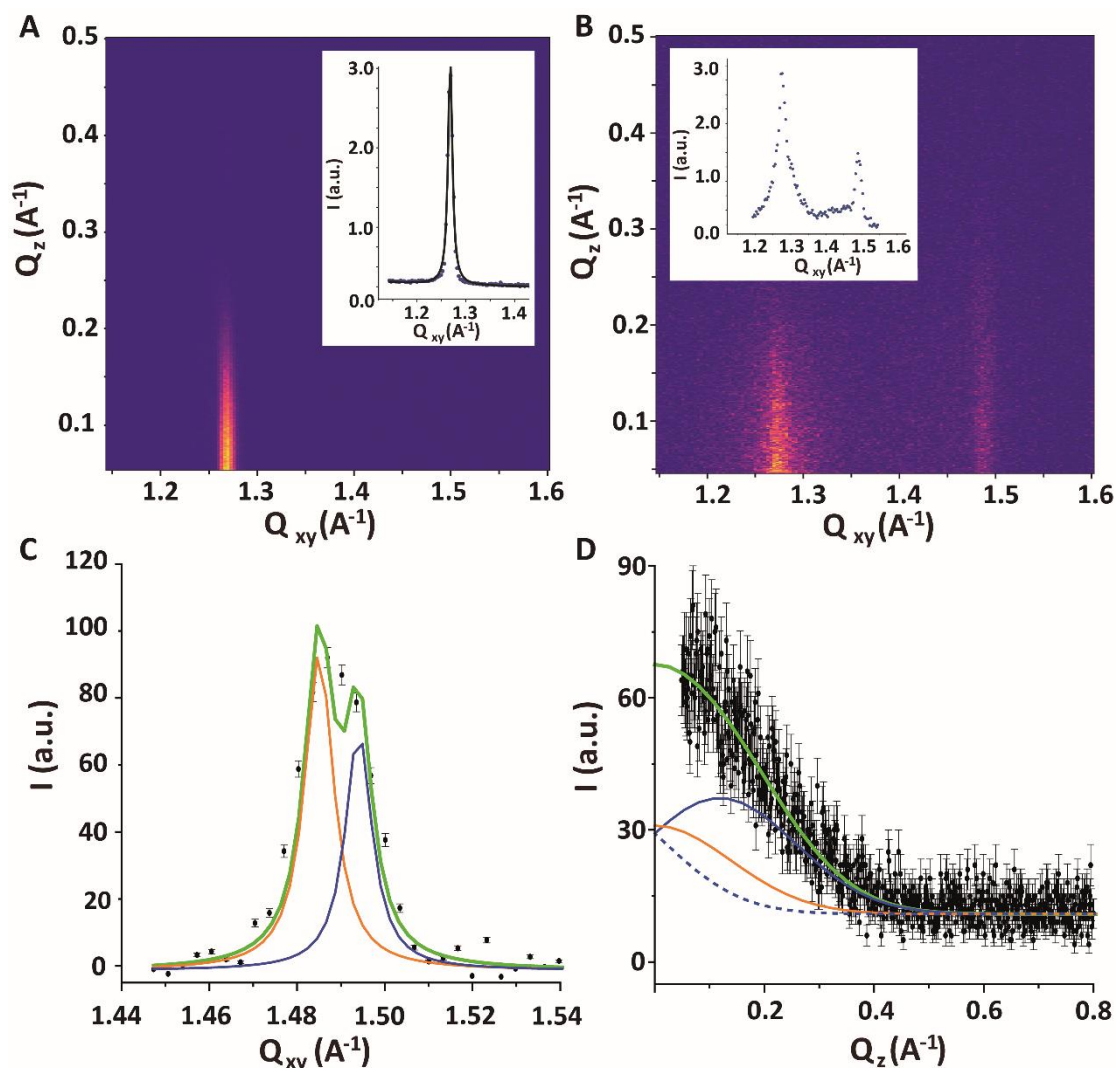


Fig. 7: (A and B) GIXD contour plot obtained (A) for a PFOL-PFOA (70:30 mol%) monolayer at $\pi = 30$ mN/m and (B) for a PFOL-PFOA monolayer after formation of a DMPC-DMPG (70:30 mol %) bilayer. Q_z – integrated intensities vs Q_{xy} are shown as insets in the respective plots. (C and D) Double-peak fit of the second intensity maximum at $Q_{xy} \approx 1.49 \text{ \AA}^{-1}$ emerging after bilayer formation. (C) Q_z – integrated intensity vs Q_{xy} , where solid lines indicate the two Lorentzian fits as well as their sum. (D) Q_{xy} – integrated intensity vs Q_z , where solid orange and blue lines indicate the modeled individual Gaussian peaks used for the model with fixed FWHM. The blue dashed curve indicates the tail of the mirror image of the blue curve, which also contributes to the intensity. The green line is the total model intensity.

4. Conclusion

In this work we have successfully formed and characterized lipid bilayers adsorbed to functionalized air/water interfaces. Ellipsometry was proven to be a suitable technique to monitor the lipid layer total thickness and thus to follow the bilayer adsorption kinetics. GIXOS and XRR provide structural details of the layer architecture, while TXRF is a powerful complementary method to deduce the bilayer coverage fraction from the P fluorescence intensity. Finally, we demonstrated that the adsorbed bilayers can be structurally characterized in in-plane direction by GIXD, which opens new possibilities for future studies, for example on the formation of glycolipid-enriched functional domains³⁷. The authors are aware of a related study by Ayscough⁶⁴ et al., which is still not published as a journal article.

Acknowledgements

We acknowledge DESY (Hamburg, Germany), a member of the Helmholtz Association HGF, for the provision of experimental facilities. Parts of this research were carried out at PETRA III and we would like to thank René Kirchhof (Chen Shen) and Milena Lippmann for assistance in using P08 and chemistry lab, respectively. Beamtime was allocated for proposals I-20191281 (June 2020) and I-20200672 (March 2021). Financial support by the German Research Foundation (DFG) via Emmy-Noether grant SCHN 1396/1 is gratefully acknowledged. We thank Giovanna Fragneto for fruitful discussions and Olaf Soltwedel for helping with XRR measurements.

References

1. M. Edidin, *Nat Rev Mol Cell Biol*, 2003, **4**, 414-418.
2. T. Heimburg, *Thermal Biophysics of Membranes*, Wiley VCH 2007.
3. T. A. Harroun, J. Katsaras and S. R. Wassall, *Biochemistry*, 2006, **45**, 1227-1233.
4. V. Rondelli, G. Fragneto, S. Motta, E. Del Favero, P. Brocca, S. Sonnino and L. Cantu, *Biochim Biophys Acta*, 2012, **1818**, 2860-2867.
5. C. Chen, F. Pan, S. Zhang, J. Hu, M. Cao, J. Wang, H. Xu, X. Zhao and J. R. Lu, *Biomacromolecules*, 2010, **11**, 402-411.
6. F. Heinrich and M. Losche, *Biochim Biophys Acta*, 2014, **1838**, 2341-2349.
7. L. A. Clifton, F. Ciesielski, M. W. Skoda, N. Paracini, S. A. Holt and J. H. Lakey, *Langmuir*, 2016, **32**, 3485-3494.
8. Y. Gerelli, L. Porcar, L. Lombardi and G. Fragneto, *Langmuir*, 2013, **29**, 12762-12769.
9. L. K. Tamm and H. M. McConnell, *Biophys J*, 1985, **47**, 105-113.
10. E. Sackmann, *Science*, 1996, **271**, 43-48.
11. F. Rehfeldt, R. Steitz, S. P. Armes, R. von Klitzing, A. P. Gast and M. Tanaka, *J Phys Chem B*, 2006, **110**, 9177-9182.
12. F. F. Rossetti, E. Schneck, G. Fragneto, O. V. Konovalov and M. Tanaka, *Langmuir*, 2015, **31**, 4473-4480.
13. O. Purrucker, A. Fortig, R. Jordan and M. Tanaka, *Chemphyschem*, 2004, **5**, 327-335.
14. S. Hertrich, F. Stetter, A. Ruhm, T. Hugel and B. Nickel, *Langmuir*, 2014, **30**, 9442-9447.
15. J. Daillant, E. Bellet-Amalric, A. Braslau, T. Charitat, G. Fragneto, F. Graner, S. Mora, F. Rieutord and B. Stidder, *Proc Natl Acad Sci U S A*, 2005, **102**, 11639-11644.
16. R. Miller, J. K. Ferri, A. Javadi, J. Krägel, N. Mucic and R. Wüstneck, *Colloid and Polymer Science*, 2010, **288**, 937-950.
17. C. Stefaniu, G. Brezesinski and H. Mohwald, *Adv Colloid Interface Sci*, 2014, **208**, 197-213.
18. G. Brezesinski and H. Möhwald, *Adv Colloid Interface Sci*, 2003, **100-102**, 563-584.

- 811 19. E. B. Watkins, C. E. Miller, W. P. Liao and T. L. Kuhl, *ACS Nano*, 2014, **8**,
812 3181-3191.
- 813 20. R. M. A. B. N. M. Azzam, *Ellipsometry and polarized light*, North-Holland :
814 Sole distributors for the USA and Canada, Elsevier Science Pub. Co.,
815 Amsterdam; New York, 1987.
- 816 21. R. Reiter, H. Motschmann, H. Orendi, A. Nemetz and W. Knoll, *Langmuir*,
817 1992, **8**, 1784-1788.
- 818 22. C. Appel, M. Kraska, C. Ruttiger, M. Gallei and B. Stuhn, *Soft Matter*, 2018,
819 **14**, 4750-4761.
- 820 23. L. G. Parratt, *Phys. Rev.*, 1954, **95**, 359-.
- 821 24. J. Als-Nielsen and D. McMorrow, *Elements of Modern X-ray Physics*, John
822 Wiley & Sons, Ltd, 2nd edn., 2011.
- 823 25. W. B. Yun and J. M. Bloch, *Journal of Applied Physics*, 1990, **68**.
- 824 26. E. Schneck, T. Schubert, O. V. Konovalov, B. E. Quinn, T. Gutsman, K.
825 Brandenburg, R. G. Oliveira, D. A. Pink and M. Tanaka, *Proceedings of*
826 *the National Academy of Sciences of the United States of America*, 2010,
827 **107**, 9147-9151.
- 828 27. G. Brezesinski and E. Schneck, *Langmuir : the ACS journal of surfaces*
829 *and colloids*, 2019, **35**, 8531-8542.
- 830 28. L. Bosio, J. J. Benattar and F. Rieutord, *Rev. Phys. Appl.*, 1987, **22**, 775 -
831 778.
- 832 29. C. A. Helm, H. Möhwald, K. Kjaer and J. Als-Nielsen, *EPL*, 1987, **4**, 697-
833 703.
- 834 30. S. Mora, J. Daillant, D. Luzet and B. Struth, *Europhysics Letters*, 2004, **66**,
835 694–700.
- 836 31. S. M. O'Flaherty, L. Wiegart, O. Konovalov and B. Struth, *Langmuir : the*
837 *ACS journal of surfaces and colloids*, 2005, **21**, 11161-11166.
- 838 32. L. Wiegart, S. M. O'Flaherty, P. Terech and B. Struth, *Soft Matter*, 2006,
839 **2**, 54-56.
- 840 33. R. Dalgliesh, *Current Opinion in Colloid & Interface Science*, 2002, **7**, 244-
841 248.
- 842 34. L. Wiegart, B. Struth, M. Tolan and P. Terech, *Langmuir : the ACS journal*
843 *of surfaces and colloids*, 2005, **21**, 7349-7357.

- 844 35. R. G. Oliveira, E. Schneck, B. E. Quinn, O. V. Konovalov, K. Brandenburg,
845 T. Gutsmann, T. Gill, C. B. Hanna, D. A. Pink and M. Tanaka, *Phys Rev E*
846 *Stat Nonlin Soft Matter Phys*, 2010, **81**, 041901.
- 847 36. M. Kanduč, E. Schneck and C. Stubenrauch, *Journal of colloid and*
848 *interface science*, 2021, **586**, 588-595.
- 849 37. T. Mukhina, G. Brezesinski, C. Shen and E. Schneck, *Journal of colloid*
850 *and interface science*, 2022, DOI: 10.1016/j.jcis.2022.01.146.
- 851 38. V. M. Kaganer, H. Möhwald and P. Dutta, *Rev. Mod. Phys.* , 1999, **71**,
852 779-819.
- 853 39. K. Kjaer, J. Als-Nielsen, C. A. Helm, L. A. Laxhuber and H. Mohwald,
854 *Physical review letters*, 1987, **58**, 2224-2227.
- 855 40. T. Broemstrup and N. Reuter, *Biophysical journal*, 2010, **99**, 825-833.
- 856 41. J. Kurniawan, J. F. Ventrici de Souza, A. T. Dang, G. Y. Liu and T. L. Kuhl,
857 *Langmuir*, 2018, **34**, 15622-15639.
- 858 42. K. Kamiya, C. Arisaka and M. Suzuki, *Micromachines (Basel)*, 2021, **12**.
- 859 43. M. Seitz, E. Ter-Ovanesyan, M. Hausch, C. K. Park, J. A. Zasadzinski, R.
860 Zentel and J. N. Israelachvili, *Langmuir : the ACS journal of surfaces and*
861 *colloids*, 2000, **16**, 6067-6070.
- 862 44. M. Tanaka, S. Kaufmann, J. Nissen and M. Hochrein, *Physical Chemistry*
863 *Chemical Physics*, 2001, DOI: 10.1039/B105007A.
- 864 45. D. Gidalevitz, Y. Ishitsuka, A. S. Muresan, O. Konovalov, A. J. Waring, R.
865 I. Lehrer and K. Y. Lee, *Proceedings of the National Academy of Sciences*
866 *of the United States of America*, 2003, **100**, 6302-6307.
- 867 46. B. Moghaddam, S. E. McNeil, Q. Zheng, A. R. Mohammed and Y. Perrie,
868 *Pharmaceutics*, 2011, **3**, 848-864.
- 869 47. D. Marsh, *Biochim Biophys Acta*, 1996, **1286**, 183-223.
- 870 48. D. F. Kienle, J. V. de Souza, E. B. Watkins and T. L. Kuhl, *Anal Bioanal*
871 *Chem*, 2014, **406**, 4725-4733.
- 872 49. M. C. Howland, A. W. Szmodis, B. Sanii and A. N. Parikh, *Biophysical*
873 *journal*, 2007, **92**, 1306-1317.
- 874 50. N. Kucerka, M. A. Kiselev and P. Balgavy, *Eur Biophys J*, 2004, **33**, 328-
875 334.
- 876 51. I. Rodriguez-Loureiro, E. Scoppola, L. Bertinetti, A. Barbetta, G. Fragneto
877 and E. Schneck, *Soft Matter*, 2017, **13**, 5767-5777.

- 878 52. C. Stefaniu, V. M. Latza, O. Gutowski, P. Fontaine, G. Brezesinski and E.
879 Schneck, *J Phys Chem Lett*, 2019, **10**, 1684-1690.
- 880 53. Y. Dai, B. Lin, M. Meron, K. Kim, B. Leahy and O. G. Shpyrko, *Journal of*
881 *Applied Physics*, 2011, **110**.
- 882 54. H. I. Petrache, S. Tristram-Nagle and J. F. Nagle, *Chem Phys Lipids*, 1998,
883 **95**, 83-94.
- 884 55. E. Schneck, F. Sedlmeier and R. R. Netz, *Proceedings of the National*
885 *Academy of Sciences of the United States of America*, 2012, **109**, 14405-
886 14409.
- 887 56. L. J. Lis, M. McAlister, N. Fuller, R. P. Rand and V. A. Parsegian,
888 *Biophysical journal*, 1982, **37**, 657-665.
- 889 57. C. Stefaniu and G. Brezesinski, *Adv Colloid Interface Sci*, 2014, **207**, 265-
890 279.
- 891 58. R. Zantl, L. Baicu, F. Artzner, I. Sprenger, G. Rapp and J. O. Rädler, *J.*
892 *Phys. Chem. B*, 1999, **103**, 10300-10310.
- 893 59. C. Sperati, in *Polymer Handbook*, eds. J. Brandrup and E. Immergut, John
894 Wiley and Sons, New York, 1989.
- 895 60. D. Jacquemain, S. Grayer Wolf, F. Leveiller, M. Lahav, L. Leiserowitz, M.
896 Deutsch, K. Kjaer and J. Als-Nielsen, *J. Phys. Colloquiums* 1989, **50**,
897 C7/29-C27/37.
- 898 61. M. Kanduc, A. Schlaich, A. H. de Vries, J. Jouhet, E. Marechal, B. Deme,
899 R. R. Netz and E. Schneck, *Nat Commun*, 2017, **8**, 14899.
- 900 62. J. Oelke, A. Pasc, A. Wixforth, O. Konovalov and M. Tanaka, *Appl. Phys.*
901 *Lett.*, 2008, **93**.
- 902 63. P. Fontaine, E. J. M. Filipe, M. C. Faure, T. Rego, S. Tassler, A. C. Alves,
903 G. M. C. Silva, P. Morgado and M. Goldmann, *Molecules*, 2019, **24**.
- 904 64. S. Ayscough, PhD, The University of Edinburgh, 2020.

905